Estimation of a matrix-fiber interface cohesive material law in FRCM-concrete joints

Tommaso D'Antino[a,*], Pierluigi Colombi[a], Christian Carloni[b], Lesley H. Sneed[c]

[a] *Politecnico di Milano, 20133 Milano, Italy*
[b] *University of Bologna, 40126 Bologna, Italy*
[c] *Missouri University of Science and Technology, Rolla, MO 65409, USA*

The application of composite materials to strengthen existing structural elements is a valid alternative to traditional strengthening techniques. Fiber reinforced cementitious matrix (FRCM) composites have been suc-cessfully employed to strengthen existing reinforced concrete (RC) and masonry structures in bending, shear, torsion, and to confine axially loaded elements. Although failure of FRCM strengthened elements depends on different parameters, such as the composite and substrate geometrical and mechanical properties, debonding at the matrix-fiber interface is generally the failure mechanism. Therefore, the study of the bond behavior of FRCM composites is a key topic to develop reliable design procedures. Numerous experimental campaigns were carried out recently to study the bond behavior of different FRCM composites. An analytical model is employed in this paper to describe the bond behavior of FRCM-concrete joints and different trilinear cohesive material laws are defined based on the experimental results. The experimental and corresponding analytical load response, strain profile, slip profile, and shear stress profile along the bonded length are compared. An analytical formulation of the bonded length needed to fully develop the stress-transfer mechanism at the matrix-fiber interface, i.e. the effective bond length, is provided for the trilinear cohesive material law employed.

Keywords:
Inorganic-matrix composites
FRCM
Analytical model
Cohesive material law

1. Introduction

The increasing need for strengthening and rehabilitation of existing structures is pushing the civil engineering community toward the research of innovative strengthening materials. Fiber reinforced composite materials represent a valid solution for strengthening existing structural elements. In the last decades, fiber reinforced polymer (FRP) composites gained great popularity due to their high strength-to-weight ratio, resistance to corrosion, and ease of installation. FRP composites may be effectively employed for flexural strengthening [1], shear strengthening [2], torsional strengthening [3], and confinement of elements mainly subjected to axial load [4]. However, the use of organic binders, usually epoxy resins, is responsible for some drawbacks of this technique, e.g. low resistance to relatively high temperature [5], difficulty of application onto wet substrates, and poor compatibility with the substrate. In order to overcome these issues, the organic resin was replaced by inorganic matrices to form fiber reinforced cementi-tious matrix (FRCM) composites. FRCM composites, which are also referred to as textile reinforced matrix (TRM) composites [6], are comprised of one or more layers of a high strength fiber net embedded within an inorganic matrix. FRCM composites were proven to be effective in flexural strengthening [7,8], shear strengthening [9,10], torsional strengthening [11], and confinement of reinforced concrete (RC) structures [12,13]. FRCM composites were also employed for strengthening of masonry elements [14], where they are particularly attractive due to their good compatibility with the substrate [15].

Failure of FRCM-concrete joints comprising one layer of reinforcing fibers is generally reported to be debonding of the fiber from the embedding matrix [16–18]. Therefore, the study of the bond behavior of an FRCM composite applied to an existing structural element is of fundamental importance to understand the complex mechanism that leads to loss of composite action. Direct-shear tests, which are widely employed to study the bond behavior of FRP composites [19,20], can be used to investigate the bond behavior of FRCM-concrete [21] and FRCM-masonry joints [22]. Debonding of FRP-concrete and FRP-ma-sonry joints is usually described as a Mode-II fracture mechanics pro-cess, and it is modeled by means of a cohesive material law (CML) associated with a zero-thickness interface [23]. Cohesive material laws have been extensively studied in the literature to describe debonding phenomena in layered materials [24–27]. In FRP-concrete and FRP-

---

* Corresponding author.
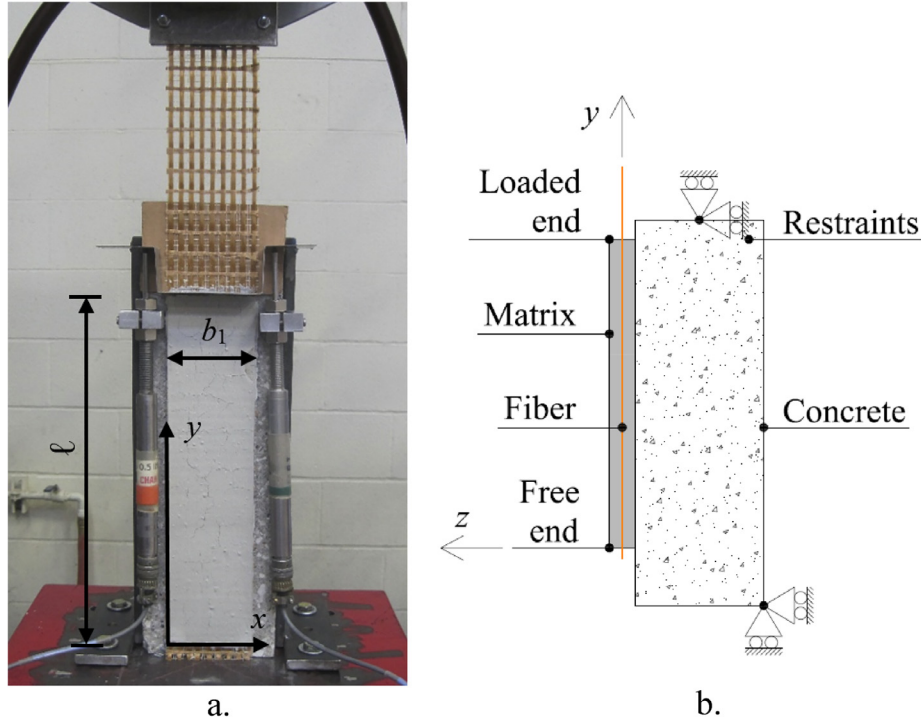*E-mail address:* tommaso.dantino@polimi.it (T. D'Antino).

Fig. 1. a) Photo of specimen DS_330_80_4 before testing. b) Sketch of the test-set-up indicating the restraints assumed.

masonry joints, the Mode-II CML is fully described by the relationship between the interfacial shear stress τ_{zy} and the corresponding slip s [28] (axes are depicted in Fig. 1). The CML associated with the FRP-substrate interface is usually comprised of an ascending branch followed by a softening branch that approaches $\tau_{zy} = 0$ when debonding occurs. The area under the τ_{zy}-s curve is the fracture energy G_F associated with the interface [29]. Following the same approach adopted for FRP composites, debonding of FRCM-concrete joints was modeled assuming a Mode-II interfacial crack propagation at the matrix-fiber interface [30]. The CML adopted to describe the FRCM matrix-fiber bond behavior does not approach $\tau_{zy} = 0$ when debonding occurs but accounts for the presence of friction (interlocking) at the debonding interface, which entails for a residual shear stress for s greater than a certain value. This residual stress, which is attributed to friction between fiber filaments and between matrix and fibers, was assumed to be constant for direct-shear tests of FRCM composites [18]. This assumption was confirmed by analytical studies of the inherent eccentricity of single-lap direct-shear tests and by numerical modeling of FRCM composite debonding with mixed-mode behavior [31,32]. The presence of friction is a pe-culiarity of FRCM-substrate joints that fail due to debonding at the matrix-fiber interface and entails for an increase of the applied load after the onset of debonding [33].

An analytical model is used in this paper to describe the bond behavior of FRCM-concrete joints that failed due to debonding at the matrix-fiber interface. The approach proposed is intended to provide an analytical solution of FRCM-concrete joints load responses up to the peak stress. Although an analytical post-peak behavior that respects the equilibrium and compatibility conditions is provided by the analytical model and discussed in the paper, it does not reproduce the post-peak behavior observed in the experimental tests. However, since FRCM strengthened elements do not generally show a post-peak behavior [7,34], the analytical model proposed can be employed to accurately obtain the behavior of FRCM strengthened structural members.

The analytical model is based on a trilinear CML that takes into account the presence of friction between fiber filaments and between matrix and fibers. The trilinear CML does not require complex calibration procedures but is simply computed using different assumptions,

as explained in Section 5. Results of different non-linear CMLs, obtained using an indirect calibration method applied to FRCM-composites, can be found in [35].

In this paper, different trilinear CMLs are calibrated starting from the results obtained by single-lap direct-shear tests on poly-paraphenylene benzo-bisoxazole (PBO) FRCM-concrete joints, which were used to compute a non-linear CML employing a fracture mechanics approach. Experimental and analytical results obtained from the trilinear CML are compared in terms of load response, strain profile, slip profile, and shear stress profile along the bonded length. A closed-form expression of the effective bond length of FRCM composites, i.e. the minimum length needed to fully develop the stress-transfer mechanism [36], associated with the trilinear CML is provided and employed to obtain the parameters of different trilinear CMLs that provide the same effective bond length.

2. Experimental results

The experimental results of PBO FRCM-concrete joints tested using a push-pull single-lap direct-shear test set-up described in [18] are compared in this paper with the analytical provisions obtained by the model proposed in [37]. The composite strip had different bonded lengths ℓ and different bonded widths b_1 and was applied on the surface of a concrete prism with 125×125 mm cross-section and length of either 375 mm or 510 mm [18]. The composite strip was comprised of one layer of a PBO fiber net with n longitudinal bundles spaced at 10 mm on center and transversal bundles, all placed on one side of the net, spaced at 20 mm on center. Fiber bundles are assumed to have a rectangular cross-section with width $b^* = 5$ mm and thickness $t^* = 0.092$ mm. The PBO fiber net was embedded between two 4 mm thick layers of a cementitious matrix specifically designed to achieve good adhesion with PBO fibers. The concrete prism was restrained whereas the fiber net, which was left bare outside the bonded area, was pulled.

Specimens were named following the notation DS_X_Y(S or D)_Z^T, where X = bonded length (in mm), Y = bonded width (in mm), S (if present) indicates that strain gauges were mounted on the fiber central

bundle, D (if present) indicates that the test was conducted until a constant load was attained, Z = specimen number, and superscript T (if present) indicates that the transversal bundles were placed toward the concrete substrate. A photo of the test set-up is shown in Fig. 1a and a sketch indicating the restraints assumed in this paper is provided in Fig. 1b [32].

Concrete and matrix cylinders were cast from the same batches used to cast the concrete prisms and composite strips, respectively, and were tested to obtain their main mechanical properties. The concrete had an average compressive and splitting tensile strength of 42.5 MPa and 3.4 MPa, respectively, whereas the matrix had an average compressive and splitting tensile strength of 28.4 MPa and 3.5 MPa, respectively [33]. The tensile strength and elastic modulus of the PBO fiber were obtained by means of tensile tests on textile specimens with different widths. The tensile strength and elastic modulus obtained were 3015 MPa and 206 GPa, respectively [30,38].

In this paper, only the results of specimens with bonded length ℓ = 330 mm and bonded width b_1 = 43 mm, 60 mm, and 80 mm were considered. Furthermore, specimens with ℓ = 330 mm that did not report an even distribution of the applied load across the composite width were disregarded [33]. Specimens considered in this paper are reported in Table 1.

The applied load P – global slip g response of specimen DS_330_80_D_4, which is representative of the load responses obtained, is depicted in Fig. 2a. In this paper g is defined as the relative displacement between the fiber and the concrete support at the loaded end. The global slip g was experimentally evaluated by averaging the displacement acquired by two LVDTs attached to the concrete support on the sides of the composite strip and reacting off of a thin aluminum Ω-shaped plate attached to the bare fiber just outside the bonded length [38].

Strain gauges were applied to the central fiber bundle along the bonded length for certain specimens (Table 1). The strain profiles $\varepsilon_{yy}(y)$ obtained (axes are depicted in Fig. 1) were fitted using a non-linear equation:

$$\varepsilon_{yy}(y) = \varepsilon_0 + \frac{\alpha + ky}{1 + e^{\frac{y - y_0}{\beta}}} \qquad (1)$$

where ε_0, α, β, and y_0 were determined using a non-linear regression analysis, whereas k depends on the matrix-fiber interfacial friction [18]. Employing a fracture mechanics approach, differentiation and integration of the fitted strain profiles allowed for obtaining the shear stress τ_{zy} and corresponding slip s, respectively, where s is the slip between points of the fibers and matrix in contact at the beginning of the test, and τ_{zy} is the corresponding interfacial shear stress. It should be noted that the global slip g coincides with s for points located at the loaded end ($y = \ell$). Combining τ_{zy} and s provided the shear stress τ_{zy} – slip s relationship, i.e. the CML, associated with the matrix-fiber

interface. Further details on the derivation of the CML can be found in [18,33].

The CML obtained for each specimen equipped with strain gauges is reported in Fig. 2b. Although specimens DS_450_60_S_1 and DS_450_60_S_2 had bonded length ℓ = 450 mm and were not considered for comparison purposes in this paper, their CMLs were included in Fig. 2b and Table 1 because the CML is fully defined for any bonded length greater than the effective bond length, which was estimated equal to 260 mm for the PBO FRCM composite considered in this paper [18]. Differences observed between the CML obtained from each specimen are caused by the randomly distributed matrix-fiber bond properties, which are also responsible for the differences between load responses of specimens with the same characteristics. An average CML, named CML_0 in the remainder of the paper, was obtained by averaging values of the shear stress corresponding to the same slip value of the CMLs obtained from each specimen equipped with strain gauges. In this paper, CML_0, which is depicted with a red line in Fig. 2b, is considered to be representative of the average matrix-fiber bond behavior and, in turn, to provide an average load response representative of the experimental load responses analyzed.

The maximum value of the shear stress and the corresponding slip of CML_0 are $\tau_{zy} = \tau_{max} = 0.77$ MPa and $s_0 = 0.18$ mm, respectively, whereas the shear stress due to friction and the corresponding slip are $\tau_{zy} = \tau_f = 0.06$ MPa and $s_f = 1.57$ mm, respectively. The fracture energy of the matrix-fiber interface obtained from CML_0 is:

$$G_F = \int_0^{s_f} \tau_{zy}(s)ds = 0.481 \text{ N/mm} \qquad (2)$$

The load response depicted in Fig. 2a shows an approximately linear behavior up to point A, which corresponds to the linear ascending branch of the associated CML. When micro-cracking starts to occur at the matrix-fiber interface, the P-g response becomes non-linear and the interface shear stress decreases. The interface shear stress continues to decrease until attaining the value associated with friction only, τ_f, at which point debonding initiates and the applied load attains P_{deb} (Fig. 2a). As the global slip g increases, the applied load P further in-creases due to the presence of friction between fiber filaments and between the matrix and fibers. The peak load value P^* is attained after the stress transfer zone (STZ), which is defined as the zone in which the stress is transferred from the matrix to the fiber by bond only, reaches the composite free end. The location and extension of the STZ at P^* depends on the shape of the CML and on the value of τ_f [32]. After P^* is attained, the applied load decreases with increasing global slip until a constant applied load P_f, which is provided by friction only, is reached.

3. Analytical model

The analytical model presented in [37] is employed in this paper to

Table 1
Results of the experimental single-lap direct-shear tests.

Name	b_1 [mm] (n)	P^* [kN]	σ^* [MPa]	Name	b_1 [mm] (n)	P^* [kN]	σ^* [MPa]
DS_330_43_2[T]	43(5)	5.25	2280	DS_330_60_D_4	60(7)	5.24	1630
DS_330_43_3	43(5)	5.27	2290	DS_330_60_D_5	60(7)	6.69	2080
DS_330_43_6	43(5)	5.09	2210	DS_330_60_S_2	60(7)	7.31	2270
DS_330_43_S_2[T]	43(5)	5.12	2230	DS_330_60_S_3	60(7)	6.55	2034
DS_330_43_S_3[T]	34(4)	3.03	1320	DS_330_80_1	80(9)	8.47	2050
DS_330_60_1[T+]	60(7)	7.05	2190	DS_330_80_3	80(9)	8.28	2000
DS_330_60_2[T]	60(7)	6.56	2040	DS_330_80_D_1	80(9)	8.90	2150
DS_330_60_3[T]	60(7)	6.06	1880	DS_330_80_D_2	80(9)	8.68	2100
DS_330_60_4[T]	60(7)	6.50	2020	DS_330_80_D_4	80(9)	8.42	2030
DS_330_60_5[T+]	60(7)	6.28	1950	DS_330_80_D_5	80(9)	8.58	2070
DS_330_60_D_1	60(7)	8.29	2570	DS_450_60_S_1[++]	60(7)	6.63	2060
DS_330_60_D_2[+]	60(7)	7.12	2210	DS_450_60_S_2[++]	60(7)	6.86	2030
DS_330_60_D_3	60(7)	6.56	2040				

[+]Not considered in the envelope curve. [++]Not considered for comparison.
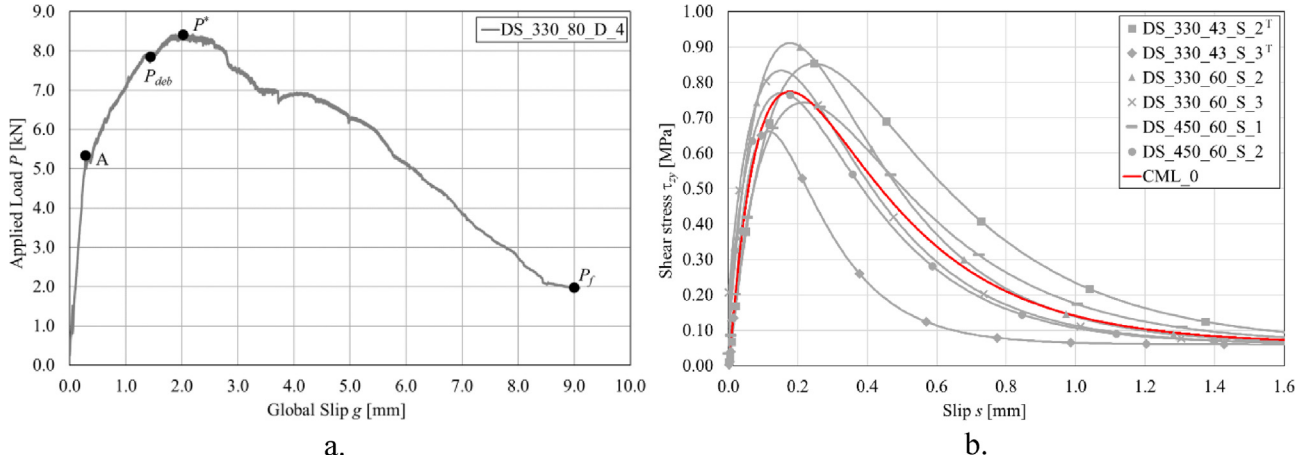
Fig. 2. a) Load response of specimen DS_330_80_D_4. b) Shear stress τ_{zy} – slip s curves obtained from specimens equipped with strain gauges.

study the load response of PBO FRCM-concrete joints using different matrix-fiber CMLs (the different CMLs are described in Section 5). It should be noted that the reference system adopted in [37] is different from that adopted in this paper. In fact, the reference system adopted in this paper is consistent with that used in the experimental work considered [18,33,38]. The analytical model assumes: i) pure Mode-II failure at the matrix-fiber interface; ii) rigid concrete and matrix (i.e. negligible deformation); iii) no width effect across the width of the composite; iv) linear elastic behavior of the fiber until failure. It should be noted that assumption (iii) is supported by experimental data [18], whereas assumption (ii), although proven acceptable to study the stress-transfer mechanism of FRCM composites [37,39,40] would need further study [33].

In this paper, a trilinear shape of the CML is assumed. The trilinear CML, which is shown in Fig. 3a, is comprised of an elastic branch with slope k_1 that ends when $\tau_{zy} = \tau_{max}$, a softening branch with slope k_2 that ends when $s = s_f$, and a horizontal friction branch with $\tau_{zy} = \tau_f$. According to load responses obtained from direct-shear and pull-out tests of inorganic-matrix composites [37,18,39,40], a minimum of three branches are needed in the CML to describe the entire bond behavior. The CML ascending branch is associated with the load response linear ascending branch, whereas the CML descending (softening) branch is associated with the load response ascending non-linear behavior. The third branch, which is assumed constant in this paper, accounts for the matrix-fiber friction observed experimentally and is responsible for the applied load increase after the onset of debonding for bonded lengths greater than the effective bond length [33].

Enforcing the equilibrium condition of an infinitesimal segment of fiber, shown in Fig. 3b, yields:
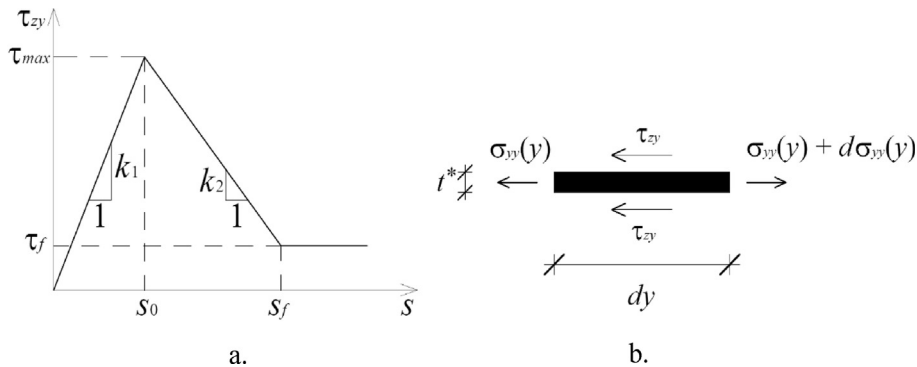
$$\tau_{zy}(y) = \frac{1}{2} Et^* \frac{d\varepsilon_{yy}(y)}{dy} \tag{3}$$

Applying the compatibility condition:

$$\varepsilon_{yy}(y) = \frac{ds(y)}{dy} \tag{4}$$

the following differential equation can be obtained:

$$\frac{d^2s}{dy^2} - \frac{2}{Et^*}\tau_{zy} = 0 \tag{5}$$

where E is the elastic modulus of the fibers. The longitudinal stress applied in the fibers at the loaded end, σ, with component along the bonded length $\sigma_{yy}(y)$ depicted in Fig. 3b, is the ratio between the applied load P and the cross-sectional area of the longitudinal fibers in the FRCM composite. Eq. (5) can be solved by assuming a CML and imposing the boundary conditions. The solution of Eq. (5) with the trilinear CML depicted in Fig. 3a requires certain assumptions and approximations. In particular, the trilinear CML adopted requires an infinite bonded length to fully develop the elastic stress-transfer mechanism. Therefore, a proper approximation of the stress-transfer mechanism should be assumed, as discussed in Section 4. Although these assumptions may be considered arbitrary, they were proved to lead to results sufficiently accurate for FRP-concrete [41] and FRCM-masonry [37] joints.

By adopting the trilinear CML of Fig. 3a, Eqs. (3)–(5) provide the interfacial shear stress $\tau_{zy}(y)$, fiber strain $\varepsilon_{yy}(y)$, and slip $s(y)$, respectively, for each point of the resulting load response. With the boundary conditions in Eq. (6), when $0 \leq s \leq s_0$ for points of the matrix-fiber interface, the load response is linear, the matrix-fiber interfacial slip is given by Eq. (7), and the corresponding strain and shear stress can be obtained by Eqs. (8) and (9), respectively:

Fig. 3. a) Trilinear CML. b) Segment of fiber with infinitesimal length dy embedded within the matrix.

$$\begin{cases} \sigma_{yy} = 0 & y = 0 \\ \sigma_{yy} = \sigma & y = \ell \end{cases} \tag{6}$$

$$s(y) = \frac{\sigma t^* \lambda}{2k_1} \frac{\cosh(\lambda y)}{\sinh(\lambda \ell)} \tag{7}$$

$$\varepsilon_{yy}(y) = \frac{\sigma t^* \lambda^2}{2k_1} \frac{\sinh(\lambda y)}{\sinh(\lambda \ell)} \tag{8}$$

$$\tau_{zy}(y) = \frac{\sigma t^* \lambda}{2} \frac{\cosh(\lambda y)}{\sinh(\lambda \ell)} \tag{9}$$

where $\lambda = \sqrt{2k_1/(E\ t^*)}$. It should be noted that since the fiber bundle thickness is negligible with respect to its width, it was disregarded when computing the matrix-fiber contact interface, i.e. the matrix-fiber contact interface was assumed equal to $2b^*$.

Eqs. (7)–(9) entail for an infinite length of the STZ associated with the elastic part of the CML. Defining an elastic effective bond length $l_{e,eff}$ as the length over which the shear stress transferred provides 97% of the applied stress corresponding to the end of the elastic behavior (point A in Fig. 2a) of a joint with infinite bonded length [41], Eqs.(7)–(9) provide:

$$l_{e,eff} = 2/\lambda \tag{10}$$

When the matrix-fiber interface slip attains s_0, microcracking occurs and the load response becomes non-linear until the onset of debonding, which corresponds to $g = s_f$ and $\sigma = \sigma_{deb}$. During this phase, points of the interface where $0 \leq s \leq s_0$ are associated with the linear ascending response of the CML [Eqs. (7)–(9)], whereas points where $s_0 \leq s \leq s_f$ are associated with the descending branch of the CML. Imposing the boundary conditions (11), Eq. (5) provides the interfacial slip, fiber strain, and interfacial shear stress associated with the descending branch [Eqs. (12)–(14)]:

$$\begin{cases} \sigma_{yy} \text{ is continuous} & y = \ell - l \\ s = s_0 & y = \ell - l \end{cases} \tag{11}$$

$$s(y) = s_0 \left\{ \frac{\lambda}{\omega} \tanh[\lambda(\ell-l)] \sin[\omega(y-\ell+l)] - \frac{k_1}{k_2} \cos[\omega(y-\ell+l)] \right.$$
$$\left. + \frac{k_1 + k_2}{k_2} \right\} \tag{12}$$

$$\varepsilon_{yy}(y) = \omega s_0 \left\{ \frac{\lambda}{\omega} \tanh[\lambda(\ell-l)] \cos[\omega(y-\ell+l)] + \frac{k_1}{k_2} \sin[\omega(y-\ell+l)] \right\} \tag{13}$$

$$\tau_{zy}(y) = -\tau_{max} \left\{ \frac{\omega}{\lambda} \tanh[\lambda(\ell-l)] \sin[\omega(y-\ell+l)] - \cos[\omega(y-\ell+l)] \right\} \tag{14}$$

where $\omega = \sqrt{2k_2/(Et^*)}$, and l is the length of the matrix-fiber interface where $s_0 \leq s \leq s_f$.

When $s \geq s_f$ the shear stress τ_{zy} is equal to τ_f, which implies that the matrix-fiber interface along which debonding has occurred is still able to sustain an axial stress equal to $2\tau_f d/t^*$, where d is the length of the debonded interface. For FRCM-concrete joints with relatively long bonded lengths, the presence of a horizontal friction branch in the CML results in an increase of the applied stress after σ_{deb} until the peak stress σ^* is attained. During this phase, for points where $s \geq s_f$, Eqs. (5) with the boundary conditions (15) yields:

$$\begin{cases} \sigma_{yy} = \sigma & y = \ell \\ s = s_f & y = \ell - d \end{cases} \tag{15}$$

$$s(y) = \frac{\tau_f}{Et^*}(y^2 - 2\ell y + l^2 - d^2) + \frac{\sigma}{E}(y - \ell + d) + s_f \tag{16}$$

$$\varepsilon_{yy}(y) = \frac{2\tau_f}{Et^*}(y - \ell) + \frac{\sigma}{E} \tag{17}$$

$$\tau_{zy}(x) = \tau_f \tag{18}$$

When $s \geq s_0$ for all points of the matrix-fiber interface, i.e. no point of the interface is associated with the linear ascending response of the CML, Eq. (5) can be solved with the boundary conditions (19), providing the solution for points where $s_0 \leq s \leq s_f$ [Eqs. (20)–(22)]:

$$\begin{cases} \sigma_{yy} = 0 & y = 0 \\ \sigma_{yy} = \sigma - 2\tau_f d/t^* & y = \ell - d \end{cases} \tag{19}$$

$$s(y) = \frac{\omega}{k_2} \left(\tau_f d - \frac{\sigma t^*}{2} \right) \frac{\cos(\omega y)}{\sin[\omega(\ell-d)]} + \tau_{max} \frac{k_1 + k_2}{k_1 k_2} \tag{20}$$

$$\varepsilon_{yy}(y) = \frac{\omega^2}{k_2} \left(\frac{\sigma t^*}{2} - \tau_f d \right) \frac{\sin(\omega y)}{\sin[\omega(\ell-d)]} \tag{21}$$

$$\tau_{zy}(y) = \omega \left(\frac{\sigma t^*}{2} - \tau_f d \right) \frac{\cos(\omega y)}{\sin[\omega(\ell-d)]} \tag{22}$$

In the case of FRP composites, the softening zone length, i.e. the zone where $s_0 \leq s \leq s_f$, remains constant as the STZ translates toward the free end [41]. For FRCM composites, the presence of friction de-termines a variation of the softening zone length as the STZ translates toward the free end, which in turns determines a non-linear decrease of the global slip as the applied stress reduces.

When debonding occurs along the entire bonded length, i.e. $s(0) = s_f$, Eq. (5) with the boundary conditions in Eq. (23) gives Eqs. (24)–(26):

$$\begin{cases} \sigma_{yy} = \sigma & y = \ell \\ s = s_f & y = 0 \end{cases} \tag{23}$$

$$s(y) = \frac{\tau_f}{Et^*}(y^2 - 2\ell y) + \frac{\sigma}{E}y + s_f \tag{24}$$

$$\varepsilon_{yy}(y) = \frac{2\tau_f}{Et^*}(y - \ell) + \frac{\sigma}{E} \tag{25}$$

$$\tau_{zy}(y) = \tau_f \tag{26}$$

4. Effective bond length

The effective bond length l_{eff} of FRP composites can be defined as the minimum length needed to fully establish the composite-substrate stress-transfer mechanism [42,43]. Additionally, l_{eff} can be defined as the length of the active bond zone where bond stresses are transferred effectively [44]. Analogously, the effective bond length of FRCM composites can be defined as the length needed to fully establish the matrix-fiber stress-transfer mechanism, i.e. as the length of the active bond zone [18,36]. In the case of FRP composites, provided that the STZ is fully established, l_{eff} can be computed as the minimum distance between points in the direction of the fibers where the strain is zero and where it reaches a constant value. In the case of FRCM composites, after the onset of debonding the presence of friction between matrix and fibers and between fiber filaments results in an increase of the fiber strain, which never reaches a constant value. However, since the effect of friction should not be taken into account if a cohesive interface is considered [29], l_{eff} of FRCM composites should be computed, provided that the STZ is fully established, as the minimum distance between points where the strain along the direction of the fiber is zero and where its derivative reaches a constant value. Alternatively, provided that the STZ is fully established, l_{eff} of FRCM composites could be computed as the distance between points in the direction of the fiber where the shear stress is zero and where it attains a constant value. It should be noted that, for FRCM composites, l_{eff} can be computed for points of the load response between P_{deb} and P^*, provided that the contribution of friction is clearly identified [36].

When points of the matrix-fiber interface are associated with slips in the range $0 \leq s \leq s_f$, the slip at the loaded end can be obtained by

setting $y = \ell$ in Eq. (12):

$$s(\ell) = s_0 \left\{ \frac{\lambda}{\omega}\tanh[\lambda(\ell-l)]\sin[\omega l] - \frac{k_1}{k_2}\cos[\omega l] + \frac{k_1 + k_2}{k_2} \right\} \qquad (27)$$

Analogously, setting $y = \ell$ in Eq. (13) and employing the fiber constitutive relationship, the applied stress at the loaded end can be obtained:

$$\sigma = \sigma_{yy}(\ell) = E\frac{ds}{dy} = \frac{2\tau_{max}}{\omega t^*}\left\{ \frac{\omega}{\lambda}\tanh[\lambda(\ell-l)]\cos[\omega l] + \sin[\omega l] \right\} \qquad (28)$$

Since debonding of the fibers from the matrix initiates at the loaded end when the interface slip attains s_f, imposing $s(\ell) = s_f$ in Eq. (27) gives:

$$\tanh[\lambda(\ell-l)] = \frac{\lambda}{\omega\sin(\omega l)}\left[\cos(\omega l) - \frac{\tau_f}{\tau_{max}} \right] \qquad (29)$$

The debonding stress can now be computed by substituting the expression of $\tanh[\lambda(\ell-l)]$ provided in Eq. (29) into Eq. (28):

$$\sigma_{deb} = \frac{2\tau_{max}}{\omega t^*}\left[\frac{1}{\sin(\omega l)} - \frac{\tau_f}{\tau_{max}}\cot(\omega l) \right] \qquad (30)$$

It can be proven that, for an infinite bonded length, the debonding stress is computed as [33]:

$$\sigma_{deb} = \frac{2\tau_{max}}{\xi \cdot t^*} \qquad (31)$$

$$\xi^2 = \frac{\tau_{max}^2}{G_F E t^*} \qquad (32)$$

The effective bond length l_{eff} can be obtained by solving Eq. (29):

$$l_{eff} = l + \frac{1}{2\lambda}\ln\frac{\omega\sin(\omega l) + \lambda[\cos(\omega l) - \tau_f/\tau_{max}]}{\omega\sin(\omega l) - \lambda[\cos(\omega l) - \tau_f/\tau_{max}]} \qquad (33)$$

where l is computed by equating Eq. (30) with Eq. (31), which gives:

$$l = \frac{2}{\omega}\arctan\left[\frac{\alpha\omega/\xi - \sqrt{(\tau_f/\tau_{max})^2 + (\alpha\omega/\xi)^2 - 1}}{\tau_f/\tau_{max} + 1} \right] \qquad (34)$$

where α is a parameter that defines the percentage of debonding stress provided by Eq. (31) and associated with l_{eff}. In other words, the effective bond length computed by Eq. (33) is the length over which the shear stress transferred provides an applied stress equal to $\alpha \cdot \sigma_{deb}$, where σ_{deb} is the applied stress associated with an infinite bonded length. It should be noted that α is needed because any CML for which $\tau(0) = 0$ and $d\tau_{zy}(0)/ds \neq \infty$ provides an infinite value of the effective bond length when employed to solve Eq. (5) [45,46]. Eqs. (10) and (34) provide an approximation of the elastic effective bond length $l_{e,eff}$ and the length l of the matrix-fiber interface where $s_0 \leq s \leq s_f$, respectively. The effective bond length obtained by adding the results of Eqs. (10) and (34), which approximate individually $l_{e,eff}$ and l, is different from that provided by Eq. (33), which is based on the approximation of the entire effective bond length.

When σ_{deb} and σ^* are known and the contribution of friction τ_f is clearly identified, the effective bond length could be estimated also using Eq. (35) [33]:

$$l_{eff} = \ell - \frac{t^*}{2\tau_f}(\sigma^* - \sigma_{deb}) \qquad (35)$$

Eq. (35) does not depend on the shape of the CML but only on the debonding and peak stress values obtained. In fact, Eq. (35) implies that the peak stress is attained when the stress transfer zone reaches the free end. However, the shape of the CML plays an important role in interface stress transfer. Thus, the results obtained with Eq. (35) should not be always considered accurate and reliable. The accuracy of Eq. (35) depends, in particular, on the shear stress associated with friction

only, τ_f. Provided that τ_f is small with respect to the shear stress associated with the matrix-fiber bond capacity, Eq. (35) can be used to obtain a close approximation of the effective bond length.

5. Results

Eight different trilinear CMLs are employed in this section to model the behavior of PBO FRCM-concrete joints using the analytical model described in Section 3. All trilinear CMLs were obtained from CML_0 (Fig. 2b), which is assumed to provide an average load response representative of the analyzed experimental load responses (Section 2), considering different assumptions. Four of them, named CML_1, 2, 3, and 4, were determined without enforcing the value of the effective bond length l_{eff}, whereas the remaining four, named CML_1L, 2L, 3L, and 4L were determined enforcing the value of l_{eff}.

It should be noted that the experimental applied stress $\sigma = P/(nt^*b^*)$ is assumed to be parallel to the longitudinal fiber. This assumption is justified by the experimental results in [32], which showed that the applied stress out-of-plane component caused by the inherent eccentricity of the single-lap direct-shear test set-up employed is negligible for the FRCM composites studied in this paper.

### 5.1. Estimation of trilinear CMLs without enforcing l_{eff}

Each trilinear CML is completely defined by enforcing four conditions. The shear stress τ_f and the fracture energy G_F of CML_1-4 were kept equal to those of CML_0, i.e. $\tau_f = 0.06$ MPa and $G_F = 0.481$ N/mm. These two conditions assure that all CMLs considered provide the same debonding stress and the same stress due to friction. Furthermore, CML_1-4 were defined by enforcing:

- CML_1: the slope k_1 and maximum shear stress τ_{max} were kept equal to those of CML_0 to provide the same slope of the linear ascending branch and applied stress associated with the end of the linear ascending branch of the load response provided by CML_0;
- CML_2: the slope k_1 and slip s_0 corresponding to the maximum shear stress were kept equal to those of CML_0 to provide the same slope of the linear ascending branch and same global slip associated with the onset of non-linear behavior of the load response provided by CML_0;
- CML_3: the maximum shear stress τ_{max} and corresponding slip s_0 were kept equal to those of CML_0 to provide the same applied stress and corresponding global slip associated with the end of the linear ascending branch of the load response provided by CML_0;
- CML_4: the slope k_1 and slip s_f corresponding to the end of the softening branch were kept equal to those of CML_0 to provide the same slope of the linear ascending branch and global slip associated with the onset of debonding of the load response provided by CML_0.

CML_0-4 are shown in Fig. 4a, whereas parameters defining the trilinear CMLs are summarized in Table 2 together with the corresponding parameters of CML_0.

An iterative procedure was employed to obtain the applied stress $\sigma = \sigma_{yy}(\ell)$ – global slip $g = s(\ell)$ curves from Eqs. (7)–(26) for each CML considered. In Fig. 4b, the analytical σ–g curves are compared with the envelope of the experimental curves obtained for specimens reported in Table 1. Specimens DS_330_60_1[T], DS_330_60_5[T], and DS_330_60_D_2, indicated in Table 1 with a superscript + at the end of the name, were not considered in the envelope because the former two reported values of the global slip along the softening branch significantly lower than those of other specimens with the same geometry, whereas the latter reported sudden drops in the load response. It should be noted that the load response associated with CML_0 is not depicted in Fig. 4b because the analytical procedure proposed is based on a trilinear shape of the CML. Load responses obtained numerically that employed the CML_0
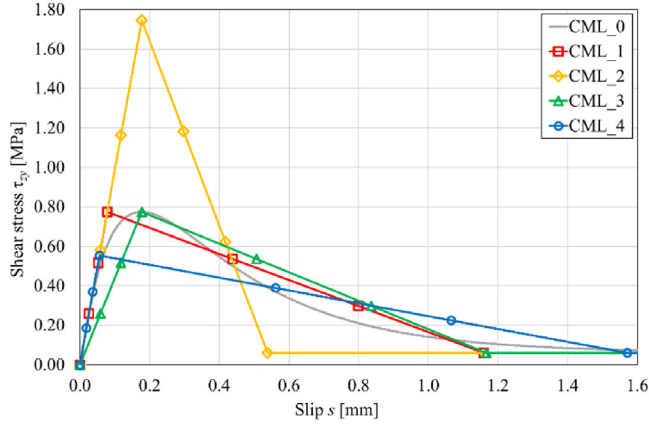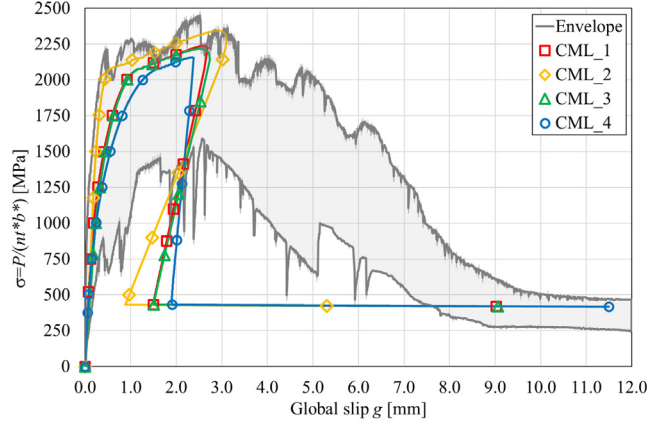
Fig. 4. a) Comparison between CML_1-4 and CML_0. b) Comparison between applied stress σ - global slip g curves obtained with CML_1-4 and the envelope of experimental results of Table 1.

Table 2
Parameters defining CML_0-4.

CML	k_1 [N/mm³]	k_2 [N/mm³]	τ_{max} [MPa]	s_0 [mm]	τ_f [MPa]	s_f [mm]	G_F [N/mm]
CML_0	9.853	–	0.77	0.18	0.06	1.57	0.481
CML_1	9.853	0.661	0.77	0.08	0.06	1.16	0.481
CML_2	9.853	4.666	1.75	0.18	0.06	0.54	0.481
CML_3	4.369	0.722	0.77	0.18	0.06	1.17	0.481
CML_4	9.853	0.326	0.55	0.06	0.06	1.57	0.481

Table 3
Results obtained with CML_0-4.

CML	σ_A [MPa]	σ_{deb} [MPa]	k_e [N/mm³]	σ^* [MPa]	$l_{eff,i}$ [mm]		
					Fig. 5a	Eq. (33)	Eq. (35)
CML_0	204[+]	2076[+]	6643	2167	260	–	260
CML_1	522	2076	6643	2237	220	211	207
CML_2	1177	2076	6643	2345	140	139	123
CML_3	784	2076	4423	2217	250	238	222
CML_4	373	2076	6643	2156	280	270	269

[+]Computed from the fracture mechanics approach proposed by [18,33].

showed good agreement with the experimental results [31].

Although the experimental results show a wide scatter, which was also observed for different FRCM composites [15], the ascending branch of analytical and experimental curves depicted in Fig. 4b are in good agreement. The post-peak behavior observed in the experimental tests, which is characterized by increasing global slip g, is different from the post-peak behavior observed in the analytical curves, where snap-back can be observed. The snap-back observed is caused by the elastic energy release of the unbonded fibers that occurs when the applied load decreases after the peak load is attained. The same snap-back phenomenon was observed in direct-shear tests on FRP-concrete joints that were tested by controlling the displacement at different points along the bonded length [47,48] and was correctly captured by analytical and numerical analysis on FRCM-concrete joints [31,35]. The analytical procedure proposed in this paper provided a post-peak behavior characterized by a snap-back phenomenon, which respects the equilibrium and compatibility conditions. The snap-back could not be obtained experimentally because tests were carried out by controlling the loaded end displacement. This control mode prevented the global slip from decreasing after the peak load was attained. A similar phenomenon of snap-back is typically observed in notched concrete beams tested in three-point bending. If the point-load deflection is used to control, the tests would be unstable after the peak of the load because of snap-back. If a clip-on gauge is used to control the CMOD (crack mouth opening displacement), the plot of the load versus point-load deflection would present snap-back [29].

Since for all CMLs considered the shear stress corresponding to friction only is equal to that of CML_0 (τ_f = 0.06 MPa), the applied stress when the fiber debonded along the entire bonded area, σ_f, is the same for all analytical curves in Fig. 4b and can be computed as:

$$\sigma_f = 2\tau_f \ell / t^* \tag{36}$$

The stress corresponding to the end of the elastic branch, named the elastic limit stress σ_A, the debonding stress σ_{deb}, and the peak stress σ^* obtained for each trilinear CML considered are listed in Table 3.

Table 3 also reports values of σ_A and σ_{deb} obtained for CML_0 applying the fracture mechanics approach proposed by [18,33]:

$$\sigma_A = \sqrt{\frac{4E \int_0^{s_0} \tau_{zy}(s)\,ds}{t^*}} \tag{37}$$

$$\sigma_{deb} = \sqrt{\frac{4EG_F}{t^*}} \tag{38}$$

The peak stress associated with CML_0 was obtained rearranging Eq. (35):

$$\sigma^* = \sigma_{deb} + \frac{2\tau_f}{t^*}(\ell - l_{eff}) \tag{39}$$

As previously observed (Section 4), Eq. (39) gives only an approximation of σ^*. However, comparison between results of experimental tests and of Eq. (39) showed that σ^* can be estimated with sufficient accuracy for the FRCM composite studied in this paper [32].

As shown by Eq. (37), σ_A depends on the area under the ascending branch of the CML. Values of σ_A obtained for CML_1, 3, and 4 are significantly smaller than the corresponding values of σ_{deb}, whereas CML_2, which is characterized by a high value of τ_{max}, provided a value of σ_A approximately equal to half of the corresponding σ_{deb} (Table 3). The global slip g corresponding to σ_A and associated with CML_2 and 3 is equal to 0.18 mm, whereas it is equal to 0.08 mm and 0.06 mm for CML_1 and CML_4, respectively. By solving Eq. (5), the slope of the linear ascending branch of the σ-g response can be obtained:

$$k_e = \frac{2k_1}{\lambda t^*}\tanh(\lambda\ell) \tag{40}$$

Values of k_e obtained are reported in Table 3 for CML_0-4. k_e corresponding to CML_0-2 and 4 are equal whereas k_e corresponding to CML_3 is lower with respect to k_e of the other CMLs considered. Since the debonding stress depends on the fracture energy G_F but not on the
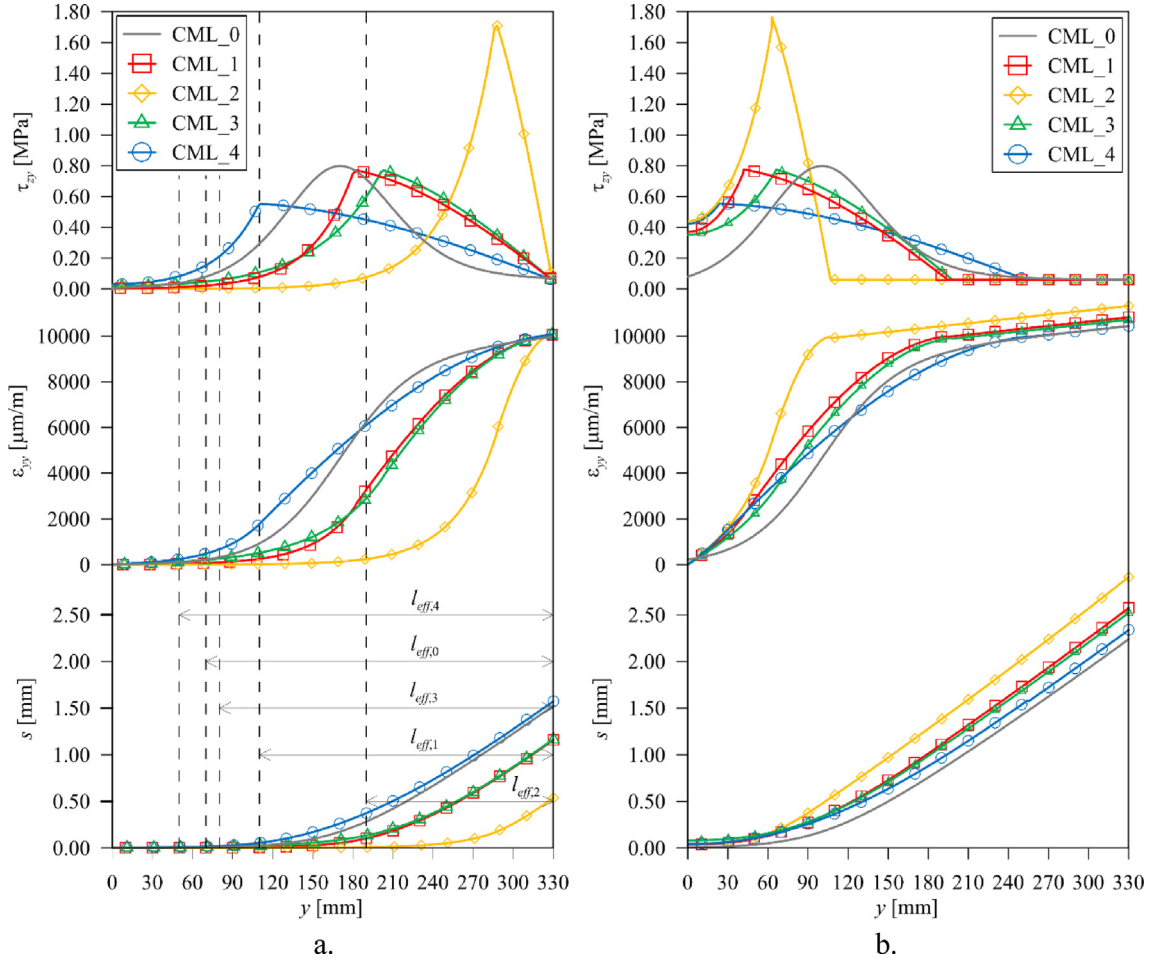
Fig. 5. Slip $s(y)$, strain $\varepsilon_{yy}(y)$, and shear stress $\tau_{zy}(y)$ along the bonded length at the debonding stress σ_{deb} (a) and at the peak stress σ^* (b).

shape of the CML [see Eq. (38)], all trilinear CMLs considered provided the same value of σ_{deb} (Table 3). Provided that the fracture energy is the same, a higher shear stress τ_{max} and slope k_1 would correspond to a lower value of the global slip corresponding to the onset of debonding, g_{deb}. Therefore, for CML_2 debonding occurred at a value of g_{deb} lower than those corresponding to CML_1, 3, and 4.

The peak stress obtained with an FRCM-concrete joint depends on its bonded length and effective bond length. Although the fracture energy associated with the trilinear CMLs is the same, differences in parameters defining each CML determine a different effective bond length and, therefore, a different peak stress σ^*. Values of σ^* obtained by CML_1-4 are reported in Table 3. Fig. 4b and Table 3 show that, for the CMLs employed, the corresponding peak stress increases with de-creasing slip associated with the onset of debonding s_f (Table 2).

Fig. 5 shows the slip $s(y)$, strain $\varepsilon_{yy}(y)$, and shear stress $\tau_{zy}(y)$ along the bonded length obtained through Eqs. (7)–(18) for CML_1-4. The shear stress and slip curves obtained by derivation and integration of CML_0 according to Eqs. (3) and (4), respectively, are included in Fig. 5 for comparison. Fig. 5a shows results for $\sigma = \sigma_{deb}$, whereas Fig. 5b shows results for $\sigma = \sigma^*$. The effective bond length determined from the strain profiles $\varepsilon_{yy}(y)$ is depicted in Fig. 5a for each CML considered and it is indicated as $l_{eff,i}$, where i is the number of the corresponding CML. $l_{eff,i}$ was estimated in Fig. 5a as the distance between the loaded end, where the derivative of the strain and the shear stress start to be con-stant, and the point where the strain is approximately equal to 3% of the strain attained at the loaded end. A similar approximation was previously employed for the analytical evaluation of the effective bond length of FRP-concrete joints, where the STZ was assumed to be associated with 97% of the applied load of a joint with infinite bonded

length [41].

Values of $l_{eff,i}$ indicated in Fig. 5a are reported in Table 3 for CML_0-4. Values of $l_{eff,i}$ obtained are different and, therefore, the peak stress associated with each CML is different. Since, given a relatively long bonded length, the applied stress increases after the onset of debonding due to the presence of friction, short effective bond lengths determine higher peak stresses with respect to long effective bond lengths. The increase in the peak stress can be observed also in terms of strain. Since the fracture energy was not varied between different CMLs, the strain in the fibers at the loaded end is equal for all CMLs at the onset of de-bonding (Fig. 5a), whereas it increases with decreasing effective bond length at the peak stress (Fig. 5b). The rate of increase of the fiber strain after the onset of debonding, $d\varepsilon/dy$, depends only on the value of τ_f and on the characteristics of the fibers and, therefore, it is equal for all CML (Fig. 5b):

$$\frac{d\varepsilon_{yy}(y)}{dy} = \frac{2\tau_f}{Et^*} \tag{41}$$

Values of the effective bond length computed with Eqs. (33) and (34) are reported in Table 3 for CML_1-4. $\alpha = 0.97$ was employed to estimate the effective bond length of FRP-concrete joints using a bi-linear CML [41]. Similar values of α were used to obtain a reasonable estimation of l_{eff} in the case of FRP composites employing different formulations of the CML [44]. However, for the FRCM-concrete joints and trilinear CML_1-4 considered in the present study, $\alpha = 0.97$ provided values of the effective bond length lower than those measured from the strain profile (Fig. 5a), with differences ranging between -17% and -36%. Therefore, α was increased to 0.999 to obtain a better estimation of l_{eff}. Values of l_{eff} obtained with $\alpha = 0.999$ (Table 3)

reported a maximum difference of -4% with respect to those measured from the strain profiles.

Finally, values of l_{eff} obtained with Eq. (35) are reported in Table 3 for each trilinear CML. The results obtained are sufficiently accurate, with the least accurate result corresponding to CML_2 (difference of -12% with respect to l_{eff} measured from the strain profile).

5.2. Estimation of trilinear CMLs with constant l_{eff}

Although the fracture energy was kept constant, CML_1-4 are associated with different values of the effective bond length and, as a consequence, lead to different peak stress values σ^* (Fig. 4b). In order to keep the same effective bond length and attain a similar peak stress, Eq. (33) can be solved numerically to obtain the relationship between λ and ω for a given value of l_{eff}.

Enforcing $l_{eff} = 260$ mm in Eq. (33) and assuming the same fracture energy $G_F = 0.481$ N/mm and friction shear stress $\tau_f = 0.06$ MPa of CML_0, the trilinear cohesive materials laws CML_1L, 2L, 3L, and 4L were computed. In addition to these assumptions, the same slope of the ascending branch k_1, slip corresponding to the maximum shear stress s_0, maximum shear stress τ_{max}, and debonding slip s_f of CML_0 were enforced for CML_1L-4L, respectively. These conditions were enforced to obtain the same slope of the linear ascending branch (CML_1L), global slip associated with the onset of non-linear behavior (CML_2L), applied stress at the end on the linear ascending branch (CML_3L), and global slip associated with the onset of debonding (CML_4L) of the load response obtained with CML_0. CML_1L-4L are depicted in Fig. 6a, whereas parameters defining them are listed in Table 4. It should be noted that, since the conditions enforced to obtain CML_2 and CML_3 led to approximately the same parameters (Table 4), CML_2L = 3L is reported in Fig. 6.

The applied stress σ - global slip g curves obtained with CML_1L-4L are compared with the envelope of experimental results considered (Table 1) in Fig. 6b. The curves obtained are in good agreement with the experimental envelope and are very similar to each other. Therefore, provided that G_F, l_{eff}, and τ_f are the same, the assumption of a different k_1, s_0, τ_{max}, or s_f does not provide significant variations of the stress transferred at the matrix-fiber interface. Similar results were obtained with bi-, tri-, and quadri-linear CMLs with the same fracture energy and effective bond length employed to describe the stress-transfer mechanism in FRP-masonry joints [49].

The stress corresponding to the onset of non-linear behavior of σ-g curves, σ_A, and the corresponding slope k_e are reported in Table 5 for CML_1L-4L. k_e depends on the slope k_1 [see Eq. (40)], and increasing k_e determines a decrease of σ_A, which in turn determines an increase of the extent of the non-linear branch. However, these differences caused

Table 4
Parameters defining CML_1L-4L.

CML	k_1 [N/mm^3]	k_2 [N/mm^3]	τ_{max} [MPa]	s_0 [mm]	τ_f [MPa]	s_f [mm]	G_F [N/mm]
CML_1L	9.853	0.420	0.63	0.06	0.06	1.41	0.481
CML_2L	4.352	0.716	0.77	0.18	0.06	1.17	0.481
CML_3L	4.309	0.724	0.77	0.18	0.06	1.17	0.481
CML_4L	40.359	0.316	0.55	0.01	0.06	1.57	0.481

Table 5
Results obtained with CML_1L-4L.

CML	σ_A [MPa]	σ_{deb} [MPa]	k_e [N/mm^3]	σ^* [MPa]	$l_{eff,iL}$ [mm]	
					Eq. (33)	Eq. (35)
CML_1L	421	2076	6643	2188	260	244
CML_2L	782	2076	4414	2216	260	223
CML_3L	782	2076	4393	2216	260	223
CML_4L	184	2076	13,444	2170	260	258

limited discrepancies between the σ-g curves obtained. The use of the same effective bond length and friction shear stress allowed for obtaining peak stress values very similar to that corresponding to CML_0 (Table 3), with a maximum difference of 2.25% associated with CML_2L = 3L (Table 5). The effective bond length $l_{eff,iL}$ obtained by Eqs.(33) and (35) is reported in Table 5 for each CML_iL. Due to the condition enforced, $l_{eff,iL}$ obtained by Eq. (33) is equal to 260 mm for all CML_iL, whereas it varies when computed with Eq. (35). These differences are due to the different shape of the CMLs employed that determines a slightly different peak stress value.

Results obtained showed that CML_1L-4L can be employed to provide good approximations of experimental load responses.

6. Conclusion

The bond behavior of FRCM-concrete joints comprised of one layer of PBO fiber net embedded within a cementitious matrix is described in this paper by means of an analytical model. A trilinear cohesive material law (CML) is adopted to describe the matrix-fiber bond relationship, and a closed-form expression of the effective bond length is provided. Different assumptions were adopted to define the trilinear CML starting from the results obtained experimentally. Analytical and experimental results are compared in terms of load response, strain profile, slip profile, and shear stress profile along the bonded length. Based on the results obtained, the following conclusions can be drawn:
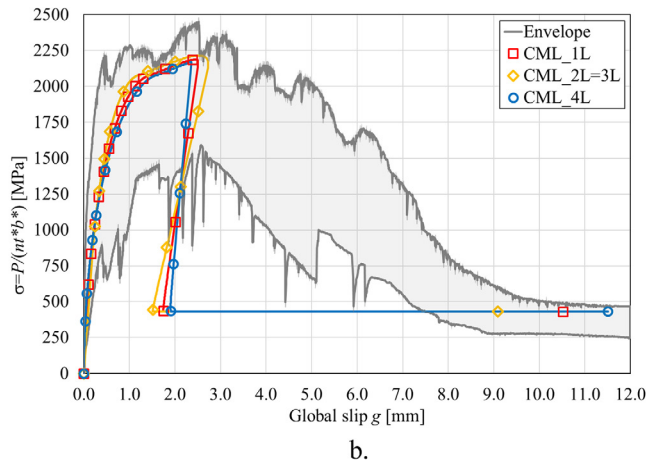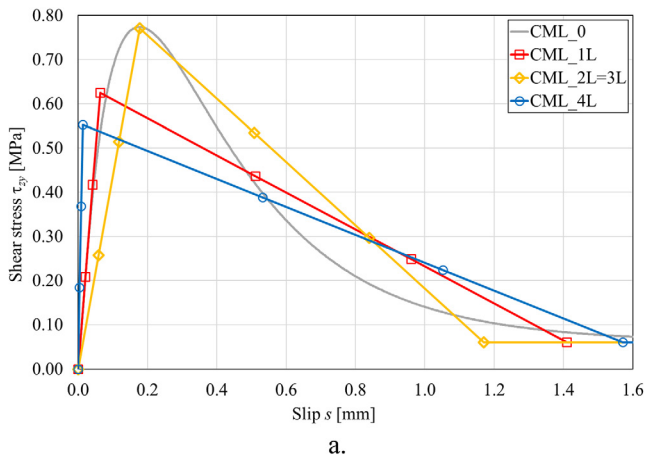

Fig. 6. a) Comparison between CML_1L-4L and CML_0. b) Comparison between applied stress σ - global slip g curves obtained with CML_1L-4L and the envelope of experimental results of Table 1.

1. The use of a trilinear CML allows for describing the load response of PBO FRCM-concrete joints up to the peak stress with adequate accuracy. The displacement control mode adopted during the experimental tests did not allow for capturing the snap-back response that is provided by the analytical solution.

2. When the experimental fracture energy and shear stress corresponding to friction are enforced in the trilinear CMLs, the debonding stress is accurately estimated. However, since the effective bond length is different for each trilinear CML, the corresponding peak stress values are different.

3. By enforcing the experimental fracture energy, shear stress corresponding to friction, and effective bond length in the trilinear CMLs, the peak stress σ^* associated with the CML obtained experimentally (CML_0) can be accurately estimated (maximum difference of 2.25%).

4. Provided that the fracture energy, shear stress corresponding to friction, and effective bond length are the same, different shapes of the trilinear CML do not lead to significant variations of the corresponding load responses.

The proposed model can be employed to study FRCM strengthened structural members, which do not generally show a post-peak behavior.

References

[1] Pellegrino C, Modena C. Flexural strengthening of real-scale RC and PRC beams with end-anchored pre-tensioned FRP laminates. ACI Struct J 2009;106(3):319–28.

[2] Khalifa A, Gold WJ, Nanni A, Abdel Aziz MI. Contribution of externally bonded FRP to shear capacity of RC flexural members. J Compos Constr 1998;2(4):195–202.

[3] Ghobarah A, Ghorbel MN, Chidiac SE. Upgrading torsional resistance of reinforced concrete beams using fiber-reinforced polymer. J Compos Constr 2002;6(4):257–63.

[4] Lam L, Teng JG. Design-oriented stress–strain model for FRP-confined concrete. Constr Build Mater 2003;17(6–7):471–89.

[5] Nigro E, Cefarelli G, Bilotta A, Manfredi G, Cosenza E. Behaviour of FRP reinforced concrete slabs in case of fire: theoretical models and experimental test. Adv Struct Eng 2012;15(4):637–52.

[6] Papanicolaou CG, Triantafillou TC, Karlos K, Papathanasiou M. Textile-reinforced mortar (TRM) versus FRP as strengthening material of URM walls: in-plane cyclic loading. Mater Struct 2007;40:1081–97.

[7] D'Ambrisi A, Focacci F. Flexural strengthening of RC beams with cement-based composites. J Comp Constr 2011;15(5):707–20.

[8] Pellegrino C, D'Antino T Experimental behavior of existing precast prestressed reinforced concrete elements strengthened with cementitious composites. Compos Part B: Eng 201355:31–40.

[9] Blanksvärd T, Täljsten B, Carolin A. Shear strengthening of concrete structures with the use of mineral-based composites. J Compos Constr 2009;13(1):25–34.

[10] Tzoura E, Triantafillou TC. Shear strengthening of reinforced concrete T-beams under cyclic loading with TRM or FRP jackets. Mater Struct 2014. http://dx.doi.org/10.1617/s11527-014-0470-9.

[11] Alabdulhady M, Sneed LH, Carloni C. Torsional behavior of RC beams strengthened with PBO-FRCM composite – an experimental study. Eng Struct 2017;136:393–405. http://dx.doi.org/10.1016/j.engstruct.2017.01.044.

[12] Ombres L. Confinement effectiveness in concrete strengthened with fiber reinforced cement based composite jackets. In: Proceedings of 8th international symposium on fiber reinforced polymer reinforcement for concrete structures, FRPRCS-8, Patras, Greece, 16–18 July 2007.

[13] Thermou GE, Katakalos K, Manos G. Concrete confinement with steel-reinforced grout jackets. Mater Struct 2015;48(5):1355–76.

[14] D'Ambrisi A, Focacci F, Caporale A. Strengthening of masonry-unreinforced concrete railway bridges with PBO-FRCM materials. Compos Struct 2013;102:193–204.

[15] De Felice G, De Santis S, Garmendia L, Ghiassi B, Larrinaga P, Lourenco PB, et al. Papanicolaou CG mortar-based systems for externally bonded strengthening of masonry. Mater Struct 2014;47:2021–37.

[16] Carozzi FG, Poggi C. Mechanical properties and debonding strength of fabric reinforced cementitious matrix (FRCM) systems for masonry strengthening. Compos Part B 2015;70:215–30.

[17] D'Ambrisi A, Feo L, Focacci F. Bond-slip relations for PBO-FRCM materials externally bonded to concrete. Compos Part B 2012;43(8):2938–49.

[18] D'Antino T, Carloni C, Sneed LH, Pellegrino C. Matrix–fiber bond behavior in PBO FRCM composites: a fracture mechanics approach. Eng Fract Mech 2014;117:94–111.

[19] Grace C, Yang Y, Sneed LH. Fracture mechanics approaches to predicting the behavior of reinforced concrete members with externally-bonded fiber reinforced polymer laminates. In A fract approach for FRP-Concr Struc, ACI SP-286, 2012, 7-1-7-20.

[20] Valluzzi MR, Oliveira DV, Caratelli A, Castori G, Corradi M, de Felice G, et al. Round robin test for composite to brick shear bond characterization. Mater Struct 2012;45:1761–91.

[21] Sneed LH, D'Antino T, Carloni C, Pellegrino C. A comparison of the bond behavior of PBO-FRCM composites determined by double-lap and single-lap shear tests. Cem Concr Compos 2015;64:37–48.

[22] Carozzi FG, Colombi P, Poggi C. Calibration of end-debonding strength model for FRP-reinforced masonry. Compos Struct 2015;120:366–77.

[23] Carloni C. Analyzing bond characteristics between composites and quasi-brittle substrates in the repair of bridges and other concrete structures [Chapter 3]. In: Kim YJ, editor. Adv Comp in Bridge Constr and Repair, Woodhead Publishing Limited, 2014, ISBN 9780857096944.

[24] Hutchinson JW, Suo Z. Mixed mode cracking in layered materials. Adv Appl Mech 1992;29:63–199.

[25] Wang H, Vu-Khanh T. Use of end-loaded-split (ELS) test to study stable fracture behaviour of composites under mode-II loading. Compos Struct 1996;36:71–9.

[26] Mazzucco G, Salomoni VA, Majorana CE. Three-dimensional contact-damage coupled modeling of FRP reinforcements - simulation of the delamination and long term process. Compos Struct 2012;110–111:15–31.

[27] Neto P, Alfaiate J, Dias-da-Costa D, Vinagre J. Mixed-mode fracture and load misalignment on the assessment of FRP-concrete bond connections. Compos Struct 2016;135:49–60.

[28] Martinelli E, Czaderski C, Motavalli M. Modeling in-plane and out-of-plane displacement fields in pull-off tests on FRP strips. Eng Struc 2011;33(12):3715–25.

[29] Bazant ZP, Planas J. Fracture and size effect in concrete and other quasibrittle materials. Boca Raton: Florida, CRC Press; 1997.

[30] D'Antino T, Sneed LH, Carloni C, Pellegrino C. Bond behavior of the FRCM-concrete interface. In Proc XI int symp on Fiber Reinforced Polymers for Reinf Concr Struct (FRPRCS11), Barros J, Sena-Cruz J Eds, 2013.

[31] Carloni C, D'Antino T, Sneed LH, Pellegrino C. 3-D numerical modeling of single-lap direct shear tests of FRCM-concrete joints using a cohesive contact damage approach. J Compos Constr. DOI 2017: 10.1061/(ASCE)CC.1943-5614.0000827.

[32] D'Antino T, Sneed LH, Carloni C, Pellegrino C. Effect of the inherent eccentricity in single-lap direct-shear tests of PBO FRCM-concrete joints. Compos Struct 2016;142:117–29.

[33] Carloni C, D'Antino T, Sneed LH, Pellegrino C. Role of the matrix layers in the stress-transfer mechanism of FRCM composites bonded to a concrete substrate. J of Eng Mech 2015;141(6).

[34] Carloni C, Bournas DA, Carozzi FG, D'Antino T, Fava G, Focacci F, et al. Fiber reinforced composites with cementitious (inorganic) matrix. Chapter 9. In: Pellegrino C, Sena-Cruz J, editors. Design procedures for the use of composites in strengthening of reinforced concrete structures. State of the art report of the RILEM TC 234-DUC, vols. 349e391. Springer; 2015. p. 501 [RILEM STAR Book Series].

[35] Focacci F, D'Antino T, Carloni C, Sneed LH. An indirect method to calibrate the interfacial cohesive material law for FRCM-concrete joints. Mater and Design 2017;128:206–17.

[36] D'Antino T, Sneed LH, Carloni C, Pellegrino C. Influence of the substrate characteristics on the bond behavior of PBO FRCM-concrete joints. Constr Build Mater 2015;101:838–50.

[37] Carozzi FG, Colombi P, Fava G, Poggi C. A cohesive interface crack model for the matrix–textile debonding in FRCM composites. Compos Struct 2016;143:230–41.

[38] Sneed LH, D'Antino T, Carloni C. Investigation of bond behavior of PBO fiber-reinforced cementitious matrix composite–concrete interface. ACI Mater J 2014;111(5):569–80.

[39] Zhang XB, Aljewifi H, Li J. Failure behaviour investigation of continuous yarn reinforced cementitious composites. Constr Build Mater 2013;47:456–64.

[40] Zhang XB, Aljewifi H, Li J. Failure mechanism investigation of continuous fibre reinforced cementitious composite by pull-out behavior analysis. In: 20th European conf on fract. Proc Mater Sci 2014;3:1377–82.

[41] Yuan H, Teng JG, Seracino R, Wu ZS, Yao J. Full-range behaviour of FRP-to concrete bonded joints. Eng Struct 2004;26:553–65.

[42] Chen JF, Teng JG. Anchorage strength models for FRP and steel plates bonded to concrete. J Struct Eng 2001;127(7):784–91.

[43] Subramaniam KV, Carloni C, Nobile L. An understanding of the width effect in FRP-concrete debonding. Strain 2011;47(2):127–37.

[44] Dai JG, Ueda T, Sato Y. Unified analytical approaches for determining shear bond characteristics of FRP-concrete interfaces through pullout tests. J Adv Concr Tech 2006;4:133–45.

[45] D'Ambrisi A, Feo L, Focacci F. Experimental analysis on bond between PBO-FRCM strengthening materials and concrete. Compos Part B 2013;44(1):524–32.

[46] Focacci F, Carloni C. Periodic variation of the transferable load at the FRP-Masonry interface. Compos Struct 2015;129:90–100.

[47] Carrara P, Ferretti D, Freddi F, Rosati G. Shear tests of carbon fiber plates bonded to concrete with control of snap-back. Eng Frac Mech 2011;79:2663–78.

[48] Colombi P, Fava G, Poggi C. End debonding of CFRP wraps and strips for the strengthening of concrete structures. Compos Struct 2014;111:510–21.

[49] Malena M, Focacci F, Carloni C, de Felice G. The effect of the shape of the cohesive material law on the stress transfer at the FRP-masonry interface. Compos Part B 2017;110:368–80.